Research Square

Preprints are preliminary reports that have not undergone peer review.
They should not be considered conclusive, used to inform clinical practice,
or referenced by the media as validated information.

A Nanoscale Pixel Architecture for High-Efficiency AlGaN Ultraviolet-C (UV-C) Light-Emitting Diodes

Sharif Sadaf

sharif.sadaf@inrs.ca

Institut National de la Recherche Scientifique (INRS)-Université du Quebec https://orcid.org/0000-0002-0136-9067

Article

Keywords: AlGaN, UV-C, microLEDs, germicidal LEDs, nanoscale pixelation, III-nitride

Posted Date: September 11th, 2026

DOI: https://doi.org/10.21203/rs.3.rs-10706593/v1

License: This work is licensed under a Creative Commons Attribution 4.0 International License.
Read Full License

Additional Declarations: There is **NO** Competing Interest.

A Nanoscale Pixel Architecture for High-Efficiency AlGaN Ultraviolet-C (UV-C) Light-Emitting Diodes

Nirmal Anand[1#], Junjie Kang[2#], Christy Giji Jenson[1], Arnob Ghosh[1], Dipon Kumar Ghosh[1], Pei-Cheng Ku[3] and Sharif Md. Sadaf[1*]

[1]*Centre Energie, Matériaux et Télécommunications, Institut national de la recherche scientifique (INRS-EMT), Varennes, Québec J3X 1P7, Canada.*

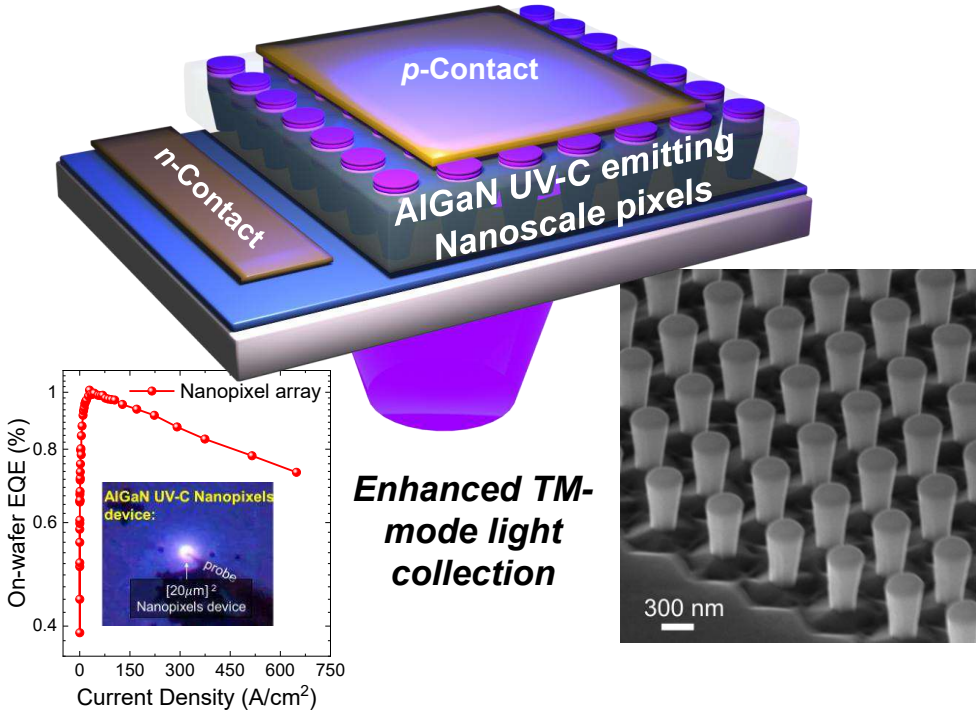
[2]*Research and Development Center for Wide Bandgap Semiconductors, Institute of Semiconductors, Chinese Academy of Sciences, Beijing 100083, China*

[3]*Department of Electrical Engineering and Computer Science, University of Michigan, Ann Arbor, Michigan 48109, United States*

#Contributed equally to this work

[*]*: E-mail : sharif.sadaf@inrs.ca*

TABLE OF CONTENT GRAPHIC



ABSTRACT:

AlGaN ultraviolet-C (UV-C) light-emitting diodes hold great promise for disinfection, water purification, and non-line-of-sight communication, yet their adoption is constrained by low external quantum efficiency (EQE) arising from high threading dislocation densities, poor *p*-type doping, and inefficient extraction of dominant transverse-magnetic (TM) polarized emission. Here, we demonstrate the first top-down fabricated ~400 nm AlGaN UV-C nanopixel array, and present a pixel-area driven experimental comparison of planar micropixel and nanopixel UV-C LEDs over a $[20\ \mu m]^2$ footprint, supported by a systematic micropixel scaling study from $[60\ \mu m]^2$ to $[20\ \mu m]^2$. The nanopixel arrays deliver peak power densities exceeding 10 W/cm^2, with an EQE of >1%. Electromagnetic simulations using the finite-difference time-domain (FDTD) method show a ~3–4× enhancement in TM-polarized light extraction compared to planar counterparts. Furthermore, Monte Carlo statistical modelling reveals a substantial reduction in dislocation density within nanoscale pixels, which further contributes to the light output enhancement of the nanopixels. These results establish top-down nanopixel architectures as a scalable route to high-efficiency UV-C emitters, identify UV-transparent sub-micrometer planarization as the key remaining materials challenge, and delineate the design space for further efficiency gains in the challenging deep UV spectral range.

Keywords: AlGaN, UV-C, microLEDs, germicidal LEDs, nanoscale pixelation, III-nitride

1. INTRODUCTION

Group III-nitrides (GaN, InN, AlN and their related alloys) semiconductors are transforming a broad range of technologies, from solid-state lighting to power electronics[1, 2], and RF/telecommunications[3] to displays[4, 5] and quantum technologies[6, 7]. Beyond these domains, the material system offers even greater promise, particularly in enabling efficient deep-ultraviolet (DUV) emission through the development of ultraviolet-C (UV-C) band light-emitting diodes (LEDs)[8, 9]. With the potential to supersede traditional UV-C gas discharge lamps, these devices offer engineered solutions that are more compact, efficient, and durable for critical applications including disinfection[10], water purification[11], spectroscopic analysis[12, 13], and non-line-of-sight (NLOS) communication[14, 15]. The strong germicidal efficacy of UV-C light (<280 nm) renders these devices highly effective for pathogen inactivation[16], making them critical for food preservation and healthcare. The growing urgency for such technologies is driven by the potential of UV-C light to help contain the spread of infectious diseases and address future global health challenges[17, 18]. At present, mercury and xenon lamps are the primary sources for UV-C applications; however, AlGaN-based UV-C LEDs have emerged as safer, more efficient alternatives that offer a compact form factor, lower energy consumption, rapid turn-on, and enhanced reliability for disinfection and sterilization systems.[10, 19, 20]

Despite such critical advantages, the efficiency of AlGaN UV-C LEDs remains substantially lower than that of their UV-A and UV-B counterparts. While UV-A LEDs consistently exhibit external quantum efficiencies (EQEs) reaching ~50%, AlGaN UV-C LEDs are typically limited to on-wafer EQEs below ~10%[21]. Three concurrent material challenges limit UV-C LED performance: (i) threading dislocation densities exceeding 10^{10} cm^{-2} in Al-rich AlGaN introduce non-radiative recombination centres and leakage currents across the quantum wells[22, 23]; (ii) optical polarization switching from transverse-electric (TE) to transverse-magnetic (TM) modes as Al content increases, combined with the high AlGaN refractive index, causes strong total internal reflection that severely limits the light

extraction efficiency (LEE) [24-26]; and (iii) the high Mg-dopant activation energy in Al-rich wide-bandgap AlGaN leads to low hole concentrations and forces use of absorptive p-GaN contact layers, further suppressing EQE[18, 27].

We have previously shown that some of these challenges can be partially overcome by fabricating AlGaN LED heterostructures grown on nanopatterned sapphire substrates (NPSS)[19, 28]. Despite this technique, the overall optoelectronic performance remains low. Recently, multiple reports demonstrated that scaling AlGaN UV-C LEDs down to micropixel geometries significantly improves TM-polarized light extraction efficiency[29-31]. Nevertheless, the overall LEE falls short for high-performance UV-C LEDs needed at the consumer/industry scale. To this end, recent advances have proposed the adoption of nanopixel geometries, which can boost LEE by several times[32, 33]. Nanopixel designs offer unique optoelectronic benefits, including improved out-coupling of TM-polarized light[34], and reduced dislocation densities[35]. However, to date, most AlGaN UV-C nanopixel devices have been realized using bottom-up epitaxial growth, relying on spontaneous formation under narrow growth windows at lower growth temperatures via plasma-assisted molecular beam epitaxy (PAMBE). Although PAMBE-grown AlGaN nanowires/nanopixels can be grown on Si [36-39], the growth technique suffers from low throughput and low EQE UV-C devices due to large densities of point and extended defects compared to metal-organic chemical vapor deposition (MOCVD) on NPSS substrates, making it less suitable for industrial-scale production.

In contrast, top-down fabricated AlGaN UV-C nanopixels have demonstrated superior light extraction performance and are more compatible with industry-scale manufacturing[32]. Top-down approaches allow the fabrication of arbitrary pixel shapes and arrays from planar AlGaN UV-C epi-layers grown under optimized MOCVD growth conditions. Despite their promise, very few studies have explored top-down fabricated AlGaN UV-C emitting nanopixels, and those that exist have been limited to pixel sizes of $\sim$1 μm[40, 41]. Furthermore, to date, there have been absolutely no experimental studies directly

comparing the performance of a planar micropixel to that of a nanopixel array architecture in UV-C LEDs over the same geometric area.

In this report, we present a comprehensive investigation on the size-dependent EQE enhancement in AlGaN UV-C micropixel LEDs, scaling pixel dimensions from [60 μm]^2 down to [20 μm]^2. In parallel, we demonstrate for the first time, a two-step top-down fabrication technique to realize UV-C emitting AlGaN nanopixel arrays on NPSS, achieving nanoscale pixel dimensions (~400 nm) arranged in a square lattice over a [20 μm]^2 footprint. While both the micropixel and nanopixel devices are fabricated within a [20 μm]^2 total area, the nanopixel array exhibits a reduced effective emitting area. Therefore, the current density for the nanopixels was also calculated considering the fill factor of the array (i.e. 400 nm diameter and 700 nm pitch; resulting in a ~0.26 fill factor in the [20 μm]^2 area). Additionally, we analyze the role of *n*-AlGaN wet etching in realizing the final nanopixel geometry, providing deeper insights into the etching mechanisms and dynamics. Through detailed finite-difference time-domain (FDTD) electromagnetic simulation and analysis, we calculate a ~4× enhancement in light extraction for the nanopixel arrays compared to planar micropixels. Experimentally, we design, fabricate and characterize [20 μm]^2 planar micropixel and nanopixel array LEDs. Although the fabricated nanopixel arrays theoretically demonstrate superior LEE, the measured EQE is found to be lower than that of the planar micropixels due to UV-C absorption losses in the spin-on glass (SOG) planarization layer. Our findings are crucial for establishing new design strategies and advancing top-down nanopixel architectures for next-generation high-efficiency UV-C emitters.

2. RESULTS AND DISCUSSION

The UV-C LED epitaxial structure was grown on 2-inch (0001)-oriented NPSS substrates using an MOCVD under optimized growth conditions[19, 28]. The device structure is identical to that used in our previous studies[19, 28], and consists of an unintentionally doped ~3 μm thick AlN buffer layer grown on a ~430 μm thick NPSS substrate (1 μm pitch, 800 nm diameter, 250 nm height), a 171 nm thick

AlN/AlGaN short-period superlattice (SPSL), a ~1.5 μm thick Si-doped *n*-type $Al_{0.60}Ga_{0.40}N$ layer, four periods of $Al_{0.52}Ga_{0.48}N/Al_{0.42}Ga_{0.58}N$ multiple quantum wells (MQWs) which are capped with a 12 nm thick Mg-doped p-type $Al_{0.84}Ga_{0.16}N$ electron blocking layer (EBL), a 60 nm thick *p*-type $Al_{0.53}Ga_{0.47}N$ layer, and a 10 nm thick heavily doped *p*-type GaN contact layer. Detailed discussion on the AlN template on NPSS and the UV-C heterostructure quality are available in Supporting Information Section S1.

Micropixel scaling enhances EQE and suppresses thermal red-shift. Several devices with $[60\ \mu m]^2$, $[40\ \mu m]^2$, and $[20\ \mu m]^2$ mesa sizes were fabricated to investigate the scaling behavior of AlGaN UV-C micropixel LEDs. The schematic of the fabricated devices and the top-view scanning electron micrograph (SEM) are shown in Figure 1 (a) and (b), respectively. The UV-C die was etched from the *p*-type GaN to the *n*-type $Al_{0.60}Ga_{0.40}N$ layer by inductively coupled plasma reactive ion etching (ICP-RIE) using an optimized Cl_2-based etch recipe. Following mesa isolation, the Ti/Au (20/40 nm) stacks were deposited around the mesa as *n*-contact. A Ni/Au (20/40 nm) metal stack was chosen for the p-contact and deposited directly onto the mesa. Further details on the micropixel fabrication are provided in the Methods section. The current density–voltage (*J–V*) characteristics of UV-C micropixel LEDs of varying sizes are shown in Figure 1 (c). All devices exhibit excellent rectification behavior with minimum reverse leakage current. Notably, smaller UV-C micropixels sustain significantly higher current densities, as shown in the semi-log J-V plot in the inset of Figure 1(c). For instance, $[20\ \mu m]^2$ micropixel reaches current densities exceeding >1 kA/cm^2. Such high current tolerance is a promising characteristic for ultrafast modulation/switching, making these compact UV-C micropixels highly suitable for high-speed deep-UV optical communication applications[42, 43].

To evaluate the emission characteristics under high injection, the current density was systematically increased from 0.1 A/cm^2 to 1 kA/cm^2. A strong size dependence in thermal behavior and spectral stability was observed. Figures 2 (a)–(c) reveal that the $[60\ \mu m]^2$ micropixel exhibited a visible red-

shift in its emission peak as the current density increased from 1 A/cm^2 to 1 kA/cm^2. In contrast, the [20 μm]^2 micropixel maintained a stable peak emission wavelength across the entire current range. To directly compare this spectral shift, the EL spectra of all three devices at 1 kA/cm² were normalized and plotted together in Figure 2 (d). The [60 μm]^2 micropixel showed a peak emission at 277.1 nm, whereas the [20 μm]^2 device peaked at 274.3 nm, corresponding to a red shift of ~4 nm. This red shift can be attributed to thermally induced bandgap shrinkage in the larger [60μm]^2 micropixel device. The absence of a similar shift in the smaller [20μm]^2 device suggests enhanced thermal dissipation due to their higher surface-to-volume ratio, and more uniform carrier injection, which minimizes localized heating.

The LOP characteristics were measured as a function of injection current density for micropixels of varying sizes, as shown in Figure 2 (e). For all devices, the LOP increases with higher injection levels; however, the current density at which the LOP begins to roll off is markedly higher in smaller micropixels. This is due to their improved current spreading and thermal management, which allow them to sustain higher current densities without significant thermal degradation. Furthermore, smaller micropixels exhibit higher LOP density compared to their larger counterparts. For example, at an injection level of 80 A/cm^2, the [60 μm]^2 device achieves ~5 W/cm^2 of output power, while the [20 μm]^2 device reaches ~10 W/cm^2, as displayed in the inset of Figure 2 (e). This enhanced performance in smaller pixels is attributed not only to improved thermal and electrical properties but also to reduced optical losses arising from device geometry. In larger micropixels (for example [60μm]^2), photons generated in the quantum wells must traverse a longer lateral path to escape the device surface. TM-polarized modes, which are dominant in UV-C Al-rich AlGaN MQW emitters due to negative crystal field splitting (-219 meV), propagate laterally and are more likely to be reabsorbed in the *p*-GaN contact layer[44]. Such waveguiding-induced reabsorption adversely affects larger mesas[30, 45], resulting in reduced extraction efficiency. The reduced dimensions also greatly modifying current spreading and

the overall light-extraction efficiency. Supporting 2D FDTD simulations show a progressive increase in relative LEE as the lateral mesa dimension is reduced from 60 to 5 μm (see Supporting Info Section 9 Figure S9). Although the simplified model does not reproduce the complete 3D device structure, it supports geometry-dependent optical extraction as an additional contributor to the enhanced performance of smaller micropixels. The extracted external quantum efficiency (EQE), shown in Figure 2 (f), further confirms these effects. The [20 μm]^2 device exhibits the highest EQE across the operating current densities, with peak efficiency achieved at slightly higher current densities than in larger [60 μm]^2 pixel. These results indicate that scaling AlGaN UV-C emitters into the nanoscale, potentially via nanostructured architectures, could further enhance the quantum efficiency.

FDTD simulations predict 3–4× light extraction enhancement for nanopixels. To probe geometry-dependent light extraction at the nanoscale, we performed 3D FDTD simulations using MEEP simulation framework[46], comparing nanopixel arrays (vertical and inverse tapered geometries) with planar micropixel AlGaN UV-C LEDs. The simulated structure consisted of a periodic square array of AlGaN nanopixels (top diameter: 400 nm; bottom diameter: 250 nm; height: 550 nm; taper angle: ~7°; pitch: 700 nm) on a 1 μm-thick sapphire substrate. As a reference, a planar [5 μm]^2 micropixel structure with identical material composition and thickness was simulated. A TM-polarized electric dipole source was placed 275 nm below the top of each nanopixel/micropixel to emulate spontaneous emission within the quantum wells. The dipole sources were excited using a Gaussian temporal profile centered at a wavelength of ~275 nm with a spectral bandwidth spanning the UV-C emission window (260–280 nm). Perfectly matched layer (PML) absorbing boundary conditions were applied at the edges of the simulation domain to eliminate artefacts and artificial reflections. The LEE was calculated by monitoring the electromagnetic power escaping the device and comparing it to the total emitted power of the dipole source. Specifically, LEE was determined by taking the ratio of the luminous flux measured by planar power monitors surrounding the simulation domain to the total flux emitted by the

dipole source. A volumetric power monitor placed in a small region (~40 nm) around the dipole was used to record the total emitted power of the source. The outward radiative flux captured by planar monitors positioned near the boundaries of the computational domain represented the extracted optical power. The LEE was therefore computed as the ratio of extracted optical power to the total emitted power. The results, shown in Figure 3 (a), reveal a pronounced enhancement in light extraction for both the vertical (taper angle: 0°) and tapered (taper angle: 7°) nanopixel geometries, exhibiting ~3-4 times higher LEE compared to the planar micropixel counterpart. This improvement is attributed to the collective effects of vertical waveguiding and sidewall tapering, which promote efficient coupling of laterally confined TM modes into substrate-directed escape cones. Further, we also investigated far field radiation patterns of the simulated structures (vertical, tapered nanopixels and micropixel geometries) to gain insights into emission directionality of the various simulated structures. The far-field radiation characteristics were computed using the near-to-far field transformation technique within the MEEP simulation framework. Figure 3 (b) shows the polar plot of the far field radiation pattern where the vertical axis corresponds to the surface normal of the simulated structures. The simulated emission pattern exhibits a characteristic two-lobed angular distribution, which is expected with TM-polarized dipole emission in high-index semiconductor structures. The tapered nanopixel structure exhibits enhanced emission within the central angular range (approximately −45° to +45°) relative to the surface normal compared to the vertical nanopixels. This actually, indicates more efficient redirection of the emitted TM-photons toward vertically propagating modes. The improved directionality arises from nanoscale waveguiding and gradual sidewall tapering effects. As a result, a larger fraction of the emitted light falls within the escape cone of the substrate, thereby contributing to the observed enhancement in light extraction efficiency. These findings are consistent with previous reports on taper-enhanced light extraction[47, 48].

Two-step top-down etch yields ~400 nm inverted-trapezoid nanopixel arrays. First, nanoscale pixel array patterns with a ~400 nm feature size and 700 nm pitch, arranged in a square lattice over an area of $[20 \times 20\ \mu\text{m}]^2$ were defined using electron beam lithography (EBL). In general, it is known that the Cl_2-based ICP-RIE is the most effective method for dry etching of III-nitride materials efficiently, which allows significantly higher etch rates and better dry etch profiles (sidewall) compared to SF_6 based chemistries[35, 49]. In the ICP-RIE process, ion bombardment, in addition to chemical etching by Cl_2 radicals, causes mechanical damage, resulting in rough, amorphous and tapered nanopixel sidewalls. The tapering of the nanopixel sidewalls is largely due to the variations in ion impact energy on the (Al)GaN surface in the ICP-RIE etch chamber[4]. This mechanical damage from the dry-etch process, leaves open bonds on the nanopixel sidewalls, creating defect sites that trap carriers. Given the significantly higher surface-area-to-volume ratio of nanopixels compared to our previously demonstrated micropixels, effective sidewall treatment becomes critical. To mitigate plasma-induced damage and passivate the sidewalls, the nanopixels were etched in a hot buffered potassium hydroxide (AZ400K) solution. Following the wet etching, the nanopixel shape transformed from a trapezoid to an inverted trapezoid profile. The chemical reactions governing the etching of the (Al)GaN heterostructure can be comprised of the following equations[50, 51]:

$$2\text{GaN} + 3\text{H}_2\text{O} \xrightarrow{\text{KOH}} \text{Ga}_2\text{O}_3 + 2\text{NH}_3 \qquad \Delta G_{298} = 1399.9\ \text{kJ/mol} \tag{1}$$

$$\text{GaN} + 3\text{H}_2\text{O} \xrightarrow{\text{KOH}} \text{Ga(OH)}_3 + \text{NH}_3 \qquad \Delta G_{298} = 723.5\ \text{kJ/mol} \tag{2}$$

$$2\text{AlN} + 3\text{H}_2\text{O} \xrightarrow{\text{KOH}} \text{Al}_2\text{O}_3 + 2\text{NH}_3 \qquad \Delta G_{298} = -350.1\ \text{kJ/mol} \tag{3}$$

$$\text{AlN} + 3\text{H}_2\text{O} \xrightarrow{\text{KOH}} \text{Al(OH)}_3 + \text{NH}_3 \qquad \Delta G_{298} = -334.2\ \text{kJ/mol} \tag{4}$$

The Gibbs free energies (ΔG_{298}) of the reactions support the favorable reaction of Al-based oxides and hydroxides. As a consequence, the AlN and Al-rich AlGaN materials are reported to have up to ~10-fold higher etch rates along *m*-plane and *a*-plane, i.e., nanopixel sidewalls, compared GaN[52]. Recent

report has also explained the crystallographic selectivity of semi-polar planes to the etchant[41]. The etch rates are further amplified in *n*-type (Al)GaN due to the high reactivity of Si dopant atoms, which are preferentially extracted from the crystal, weakening the surrounding lattice bonds and accelerating dissolution of (Al)Ga and N atoms[53]. These combined effects, i.e., crystallographic selectivity, doping sensitivity, and enhanced chemical reactivity of *n*-type Al-rich AlGaN, collectively lead to the formation of the observed inverted-trapezoid nanopixel profiles after KOH wet etching, as shown in the scanning electron micrograph (SEM) in Figure 4 (a). To further investigate the structural quality of the nanopixel sidewalls after the wet etching treatment, high-angle annular dark-field scanning transmission electron microscopy (HAADF-STEM) was performed. The cross-sectional HAADF-STEM image shown in Figure 4 (d) reveals crystalline UV-C AlGaN nanopixel sidewalls with uniform contrast, indicating that the underlying AlGaN crystal lattice remains highly ordered after the wet etching process. Importantly, no amorphous/damage layer or extended defect formation is observed along the etched sidewalls, suggesting that the KOH treatment effectively removes the plasma-induced surface damage introduced during the dry etch step. A higher magnification HAADF-STEM image of the region highlighted by the red dashed box in Figure 4 (d) is presented in Figure 4 (e), showing the active region of the nanopixel. Detailed information regarding the nanopixel formation and device fabrication is provided in Supporting Information Sections S1 and S2.

SOG planarization limits nanopixel EQE through parasitic UV-C absorption. The fabricated nanopixel devices were characterized by measuring their *J–V* characteristics, as shown in Figure 5 (a). For comparison, the planar [20 μm]^2 micropixel *J–V* characteristics are plotted in the same graph. The *J–V* curve of the nanopixel exhibits excellent diode rectification behavior, with leakage currents comparable to the planar micropixel up to –5 V. The nanopixel device tolerates current densities up to 10^4 A/cm^2, which is an order of magnitude higher compared to the planar micropixel device. However, a slight sub-threshold turn-on is observed in the forward bias region, as can be seen in the inset of

Figure 5 (a). This behavior is likely due to current leakage paths formed at residual openings in the spin-on glass (SOG) layer post the etch-back step, as seen in the inset of high-magnification SEM of the etched-back UV-C nanopixel array in Figure 4 (b). Further nanopixel device *J-V* characterization results and discussions are provided in Supporting Information Section S4.

The EL spectra emission was collected normal to the device surface using a fiber coupled to a UV–visible spectrometer. Figure 5 (b) shows the EL spectra under increasing injection current densities, showing stable and bright UV-C emission with no significant thermal degradation and/or peak shift. Figure 5 (c) compares the EL spectra of the nanopixel and planar micropixel devices at a high 1000 A/cm^2 current density.

The LOP characteristics of the [20 μm]^2 nanopixel devices were measured and benchmarked against planar [20 μm]^2 micropixel device. As shown in Figure 6 (a), the nanopixel device achieves >10 W/cm^2 in LOP density. Counterintuitively, this value is ~4× lower than that of the micropixel planar device, despite FDTD simulations predicting significantly enhanced LEE for the nanopixel array/geometry. On-wafer EQE measurements further reveal a reduced peak EQE of 1.01% for the nanopixel, in contrast to 2.59% for the planar counterpart, as inferred in Figure 6 (b). While EQE is classically defined as the product of internal quantum efficiency (IQE) and LEE, the observed lower EQE for nanopixels, despite their geometrically enhanced LEE (and their reduced effective active region), indicates that additional optical losses dominate that outweigh the nanopixel design benefits.

One such detrimental efficiency loss mechanism may stem from threading dislocations (TDs) in the AlGaN UV-C heterostructure, which are well known to act as nonradiative recombination centers (NRCs) and also promote the formation of point defects in the vicinity of the TDs[22]. We performed Monte Carlo simulations[35] to statistically evaluate the probability of dislocations present in the individual nanopixels (see Supporting Information Section S8). Our simulations show that ~60% of 400 nm nanopixels are dislocation-free, whereas the 20 μm planar micropixel is essentially 0%

dislocation-free. These results demonstrate the key statistical advantage of nanoscale pixelation in mitigating TD-induced recombination losses.

As a result, the discrepancy in EQE performance between the nanopixel and micropixel device can be predominantly explained by the parasitic absorption from the SOG planarization layer. Although the nanopixels have significantly higher surface area-to-volume ratio, the role of sidewall related nonradiative recombination is expected to be less pronounced in AlGaN based UV devices than in InGaN based visible emitters[54]. UV–visible absorption spectroscopy, as shown in Figure 6 (c), reveals that a bare UV-C LED die exhibits absorption of ~0.05 at 275 nm, whereas the same die coated with SOG (cured) shows significantly increased absorption of ~0.15; i.e. a 3× increase in absorption of UV-C light. Figure 6 (d) overlays the normalized absorption profile with normalized EL spectra to emphasize the spectral overlap and corresponding SOG-induced absorption loss. The residual absorption is likely due to incomplete removal of organic and silanol species during curing, which are known to absorb strongly below 300 nm wavelengths[55-57]. Additional EQE measurements for other nanopixel devices, along with characterization (experimental setup) and benchmarking against state-of-the-art UV-C LEDs, are provided in Supporting Information Sections S5–S7.

This analysis reveals a critical trade-off in nanopixel-based UV-C emitters; while the demonstrated inverted-trapezoid nanopixel improves emission directionality and TM-mode light extraction, the benefits are presently constrained by optical losses in non-ideal spin-on dielectric materials (i.e. SOG). Although CYTOP and similar fluoropolymer-based encapsulants offer excellent UV transparency[58], no comparably transparent dielectric exists for high-resolution planarization. Incorporating a fully UV-transparent planarization dielectric would allow the intrinsic LEE enhancements of the nanopixel geometry to be fully realized. In summary, our results highlight both the potential and current limitations of the presented ultra-dense UV-C nanopixel architectures for high energy UV-C photon extraction.

3. CONCLUSION

This study presents a systematic analysis of scaling effects on the performance of AlGaN-based UV-C LEDs, demonstrating that smaller [20 μm]^2 micropixels offer improved thermal management, higher current tolerance, and enhanced EQE compared to larger pixels. Although these smaller [20 μm]^2 micropixels produce lower absolute LOP, their significantly higher LOP density enables high total output when integrated into large-scale micropixel arrays, making them particularly well-suited for disinfection applications. We also demonstrated, for the first time, a ~400 nm top-down fabricated AlGaN UV-C emitting nanopixel arrays, with a 1.01% peak external quantum efficiency. Our detailed FDTD simulations show significant light extraction benefits (>50% increase in LEE compared to planar micropixel geometry of the identical area) from the demonstrated nanopixel architecture. Furthermore, the nanopixels displayed excellent diode rectification characteristics, spectral stability, and output power densities exceeding 10 W/cm^2, which show strong potential for next-generation UV-C emitters. This work lays the foundation for a top-down scalable, next-generation, sub-500 nm nanoscales UV-C emitters with enhanced optical performance.

METHODS

AlGaN Micropixel UV-C LED Fabrication. The AlGaN UV-C micropixel fabrication is as follows. First, the UV-C die was solvent cleaned, and spin coated with a positive photoresist (Shipley S1805) and baked. Photolithography was performed to define several [20 μm]^2, [40μm]^2, and [60μm]^2 square mesas. After development, ~80 nm Ni was e-beam evaporated on the UV-C die and lifted-off. The sample was then etched to isolate the mesas using an optimized Cl_2 based ICP-RIE recipe. Subsequently, two photolithographic steps were performed, for the *n*-contact (Ti/Au (20/40 nm)) and *p*-contact (Ni/Au (20/40 nm)). Finally, the metal-contacts were annealed at 500°C for 5 min in N_2 ambient.

AlGaN Nanopixel UV-C LED Fabrication. For nanopixel formation, the UV-C LED die was first solvent cleaned and spin-coated with a high-resolution positive electron-beam resist (PMMA 950k). A square lattice of circular patterns, each 400 nm in diameter and confined within a $[20\ \mu m]^2$ area, was defined using electron-beam lithography (EBL). After development, the sample was O_2 plasma ashed to remove residual resist. An ~80 nm Ni layer was deposited via e-beam evaporation and lifted off to act as an etch mask. The underlying UV-C LED layers were then etched down to the *n*-AlGaN using a Cl_2-based ICP-RIE process, forming nanopixels of ~600 nm in height. To remove plasma-induced sidewall damage, the sample was etched in a buffered potassium hydroxide (AZ400K) solution at ~80°C. The nanopixel array was then planarized using spin-on glass (SOG), which was thermally cured at 400°C in N_2 ambient for ~2 hours with controlled temperature ramping to avoid thermal shock and cracking. The cured SOG layer was etched back using CF_4-based ICP dry etching to expose the top *p*-GaN contact surface. Patterning was then performed to open vias to the *n*-AlGaN by wet etching the SOG in buffered oxide etch (BOE). Finally, *p*- and *n*-type metal contacts were patterned and deposited using standard photolithographic and e-beam deposition processes.

Device Characterization. The I−V characteristics of the various device were measured under continuous-wave (CW) bias with a Keithley 2400 source meter unit (SMU). The electroluminescence was collected normal to the device surface, through a fiber and routed to a UV-Visible spectrometer (Ocean Optics USB2000+). For light output power and EQE measurements, the micropixel and nanopixel devices were probed from the top and the light was collected from backside of the rough sapphire substrate into a UV extended photodiode (Thorlabs S120VC). All electrical measurements of the micropixel and nanopixel devices were performed under CW biasing conditions, on-wafer and at room temperature (~300 K) with no heat sink or active cooling.

ACKNOWLEDGEMENTS

This work was supported by the Natural Sciences and Engineering Research Council of Canada (NSERC) through Discovery and Quantum Alliance Grant programs, MEIE Photonique Quantique Quebec (PQ2) program, and the Canada Research Chair program.

REFERENCES

1. Y. Zhang, F. Udrea and H. Wang, Nature Electronics **5** (11), 723–734 (2022).

2. C.-C. Tu, C.-L. Hung, K.-B. Hong, S. Elangovan, W.-C. Yu, Y.-S. Hsiao, W.-C. Lin, R. Kumar, Z.-H. Huang, Y.-H. Hong, Y.-K. Hsiao, R.-H. Horng, B.-Y. Tsui, T.-L. Wu, J.-H. He and H.-C. Kuo, Nature Reviews Electrical Engineering **1** (7), 435–452 (2024).

3. Y. Zhang, A. Zubair, Z. Liu, M. Xiao, J. Perozek, Y. Ma and T. Palacios, Semiconductor Science and Technology **36** (5) (2021).

4. M. Sheen, Y. Ko, D. U. Kim, J. Kim, J. H. Byun, Y. Choi, J. Ha, K. Y. Yeon, D. Kim, J. Jung, J. Choi, R. Kim, J. Yoo, I. Kim, C. Joo, N. Hong, J. Lee, S. H. Jeon, S. H. Oh, J. Lee, N. Ahn and C. Lee, Nature **608** (7921), 56–61 (2022).

5. J. Park, J. H. Choi, K. Kong, J. H. Han, J. H. Park, N. Kim, E. Lee, D. Kim, J. Kim, D. Chung, S. Jun, M. Kim, E. Yoon, J. Shin and S. Hwang, Nature Photonics **15** (6), 449–455 (2021).

6. M. J. Holmes, K. Choi, S. Kako, M. Arita and Y. Arakawa, Nano Lett **14** (2), 982–986 (2014).

7. J. Luo, Y. Geng, F. Rana and G. D. Fuchs, Nat Mater **23** (4), 512–518 (2024).

8. D. Cameron, P. M. Coulon, S. Fairclough, G. Kusch, P. R. Edwards, N. Susilo, T. Wernicke, M. Kneissl, R. A. Oliver, P. A. Shields and R. W. Martin, Nano Lett **23** (4), 1451–1458 (2023).

9. M. Kneissl, T.-Y. Seong, J. Han and H. Amano, Nature Photonics **13** (4), 233–244 (2019).

10. M. Biasin, A. Bianco, G. Pareschi, A. Cavalleri, C. Cavatorta, C. Fenizia, P. Galli, L. Lessio, M. Lualdi, E. Tombetti, A. Ambrosi, E. M. A. Redaelli, I. Saulle, D. Trabattoni, A. Zanutta and M. Clerici, Sci Rep **11** (1), 6260 (2021).

11. M. Kneissl, T. Kolbe, C. Chua, V. Kueller, N. Lobo, J. Stellmach, A. Knauer, H. Rodriguez, S. Einfeldt, Z. Yang, N. M. Johnson and M. Weyers, Semiconductor Science and Technology **26** (1) (2011).

12. S. K. Piendl, D. Geissler, L. Weigelt and D. Belder, Anal Chem **92** (5), 3795–3803 (2020).

13. F. Feng, Y. Liu, K. Zhang, M. Zhanghu, K.-W. Chan, K. Xu, H.-S. Kwok and Z. Liu, Applied Physics Letters **121** (22) (2022).

14. P. Tian, X. Shan, S. Zhu, E. Xie, J. J. D. McKendry, E. Gu and M. D. Dawson, IEEE Journal of Quantum Electronics **58** (4), 1–14 (2022).

15. L. Guo, Y. Guo, J. Yang, J. Yan, J. Liu, J. Wang and T. Wei, IEEE Photonics Journal **14** (1), 1–5 (2022).

16. M. Ploydaeng, N. Rajatanavin and P. Rattanakaemakorn, Photodermatol Photoimmunol Photomed **37** (1), 12–19 (2021).

17. B. K. SaifAddin, A. S. Almogbel, C. J. Zollner, F. Wu, B. Bonef, M. Iza, S. Nakamura, S. P. DenBaars and J. S. Speck, ACS Photonics **7** (3), 554–561 (2020).

18. A. Pandey, J. Gim, R. Hovden and Z. Mi, Applied Physics Letters **117** (24) (2020).

19. W. Luo, S. M. Sadaf, T. Ahmed, M. Z. Baten, M. O. Faruque, M. A. Hossain, H. Wang, Y. Li, Y. Yuan, W. Wang, S. Liu, T. Li, Q. Wang, J. Kang and X. Wang, ACS Photonics **9** (9), 3172–3179 (2022).

20. M. Raeiszadeh and B. Adeli, ACS Photonics **7** (11), 2941–2951 (2020).

21. Y. Yao, H. Li, P. Li, C. J. Zollner, M. Wang, M. Iza, J. S. Speck, S. P. DenBaars and S. Nakamura, Applied Physics Express **15** (6) (2022).

22. D. Cameron, P. R. Edwards, F. Mehnke, G. Kusch, L. Sulmoni, M. Schilling, T. Wernicke, M. Kneissl and R. W. Martin, Applied Physics Letters **120** (16) (2022).

23. M. Moseley, A. Allerman, M. Crawford, J. J. Wierer, M. Smith and L. Biedermann, Journal of Applied Physics **116** (5) (2014).

24. T. Takano, T. Mino, J. Sakai, N. Noguchi, K. Tsubaki and H. Hirayama, Applied Physics Express **10** (3) (2017).

25. M. Guttmann, A. Susilo, L. Sulmoni, N. Susilo, E. Ziffer, T. Wernicke and M. Kneissl, Journal of Physics D: Applied Physics **54** (33) (2021).

26. J. Li, J. Wang, Y. Zhang, J. Yan and Y. Guo, Journal of Nanophotonics **12** (04) (2018).

27. X. Qiu, Y. Chen, E. Han, Z. Lv, Z. Song and H. Jiang, Materials Advances **1** (1), 77–85 (2020).

28. N. Anand, J. Kang, B. Sikder, C. G. Jenson, M. Z. Baten and S. M. Sadaf, ACS Applied Electronic Materials **7** (1), 417–423 (2024).

29. J. W. Lee, J. H. Park, D. Y. Kim, E. F. Schubert, J. Kim, J. Lee, Y.-l. Kim, Y. Park and J. K. Kim, ACS Photonics **3** (11), 2030–2034 (2016).

30. R. Floyd, M. Gaevski, K. Hussain, A. Mamun, M. V. S. Chandrashekhar, G. Simin and A. Khan, Applied Physics Express **14** (8) (2021).

31. J. Rass, H. K. Cho, M. Guttmann, D. Prasai, J. Ruschel, T. Kolbe and S. Einfeldt, Applied Physics Letters **122** (26) (2023).

32. T. Wei, S. M. Islam, U. Jahn, J. Yan, K. Lee, S. Bharadwaj, X. Ji, J. Wang, J. Li, V. Protasenko, H. Xing and D. Jena, Optics Letters **45** (1) (2019).

33. E. Lopez-Fraguas, F. Binkowski, S. Burger, S. Hagedorn, B. Garcia-Camara, R. Vergaz, C. Becker and P. Manley, Sci Rep **12** (1), 11480 (2022).

34. L. Zhang, Y. Guo, J. Yan, Q. Wu, Y. Lu, Z. Wu, W. Gu, X. Wei, J. Wang and J. Li, Photonics Research **7** (9) (2019).

35. G. T. Wang, Q. Li, J. J. Wierer, D. D. Koleske and J. J. Figiel, physica status solidi (a) **211** (4), 748–751 (2014).

36. S. M. Sadaf, S. Zhao, Y. Wu, Y. H. Ra, X. Liu, S. Vanka and Z. Mi, Nano Lett **17** (2), 1212–1218 (2017).

37. X. Liu, B. H. Le, S. Y. Woo, S. Zhao, A. Pofelski, G. A. Botton and Z. Mi, Optics express **25** (24), 30494–30502 (2017).

38. H. Sun, J. Yin, E. F. Pecora, L. Dal Negro, R. Paiella and T. D. Moustakas, IEEE Photonics Journal **9** (4), 1–9 (2017).

39. T. Wei, S. Islam, U. Jahn, J. Yan, K. Lee, S. Bharadwaj, X. Ji, J. Wang, J. Li and V. Protasenko, Optics Letters **45** (1), 121–124 (2019).

40. B. Melanson, M. Hartensveld, C. Liu and J. Zhang, AIP Advances **11** (9) (2021).

41. M. Hartensveld, B. Melanson, C. Liu and J. Zhang, Journal of Physics: Photonics **3** (2) (2021).

42. D. Li, S. Liu, Z. Qian, Q. Liu, K. Zhou, D. Liu, S. Sheng, B. Sheng, F. Liu, Z. Chen, P. Wang, T. Wang, X. Rong, R. Tao, J. Kang, F. Chen, J. Kang, Y. Yuan, Q. Wang, M. Sun, W. Ge, B. Shen, P. Tian and X. Wang, Adv Mater **34** (19), e2109765 (2022).

43. E. Xiong, Y. Huang, M. Luo and W. Zhang, Physica Scripta (2026).

44. J. Li, K.-B. Nam, M. L. Nakarmi, J.-Y. Lin, H. Jiang, P. Carrier and S.-H. Wei, Applied Physics Letters **83** (25), 5163–5165 (2003).

45. F. Feng, Y. Liu, K. Zhang, H. Yang, B.-R. Hyun, K. Xu, H.-S. Kwok and Z. Liu, Nature Photonics **19** (1), 101–108 (2024).

46. A. F. Oskooi, D. Roundy, M. Ibanescu, P. Bermel, J. D. Joannopoulos and S. G. Johnson, Computer Physics Communications **181** (3), 687–702 (2010).

47. B. Melanson, M. Seitz and J. Zhang, IEEE Photonics Journal **14** (6), 1–10 (2022).

48. R. Lin, S. V. Galan, H. Sun, Y. Hu, M. S. Alias, B. Janjua, T. K. Ng, B. S. Ooi and X. Li, Photonics Research **6** (5) (2018).

49. N. Yulianto, A. D. Refino, A. Syring, N. Majid, S. Mariana, P. Schnell, R. A. Wahyuono, K. Triyana, F. Meierhofer, W. Daum, F. F. Abdi, T. Voss, H. S. Wasisto and A. Waag, Microsyst Nanoeng **7**, 32 (2021).

50. W. Guo, R. Kirste, I. Bryan, Z. Bryan, L. Hussey, P. Reddy, J. Tweedie, R. Collazo and Z. Sitar, Applied Physics Letters **106** (8) (2015).

51. B. Kazanowska, K. Sapkota, B. Gunning, K. Jones and G. Wang, *Exploring AlGaN nanostructures fabricated via chemical wet etching*. (SPIE, 2021).

52. B. A. Kazanowska, University of Florida, PhD Thesis, 2021.

53. M. Behzadirad, M. Nami, N. Wostbrock, M. R. Zamani Kouhpanji, D. F. Feezell, S. R. J. Brueck and T. Busani, ACS Nano **12** (3), 2373–2380 (2018).

54. Y. Yao, H. Li, P. Li, C. J. Zollner, M. Wang, M. Iza, J. S. Speck, S. P. DenBaars and S. Nakamura, Applied Physics Express **15** (6), 064003 (2022).

55. J. Y. Bae, Y. Kim, H. Kim, Y. Kim, J. Jin and B. S. Bae, ACS Appl Mater Interfaces **7** (2), 1035–1039 (2015).

56. A. Fang, J. Liu, Z. Du, P. Tang, Y. Xie, W. Guo, H. Xu and J. Sun, Applied Physics Letters **125** (2) (2024).

57. K. Karaste, Masterthesis, Aalto University School of Science and Technology (2010).

58. T. Ogawa and Y. Hanada, Applied Physics A **122** (3) (2016).

FIGURE CAPTIONS

Figure 1. (a) Schematic illustration of the top-down fabricated AlGaN UV-C micropixel LED device. (b) Top-view SEM image of a fabricated micropixel device with varying mesa sizes ([60 μm]^2, [40 μm]^2 and [20 μm]^2). All the scale bars correspond to 40 μm length. (c) The current density-voltage (*J–V*) characteristics of micropixels with different sizes, showing excellent rectification and higher current tolerance in smaller devices. Inset: Semi-log scale plot depicting the leakage currents of the micropixel devices.

Figure 2. (a–c) Electroluminescence (EL) spectra of [60 μm]^2, [40 μm]^2, and [20 μm]^2 micropixels, respectively, under increasing injection current densities from 0.1 to 1000 A/cm^2. (d) Normalized EL spectra at 1000 A/cm^2 illustrating a red-shift of ~4 nm in the [60 μm]^2 device due to thermal effects, absent in smaller [20 μm]^2 pixels.

Figure 3. (a) Light output power (LOP) versus current density for micropixel LEDs of different sizes. Inset: LOP values at 80 A/cm^2, showing enhanced emission from [20 μm]^2 device. (b) Extracted external quantum efficiency (EQE) as a function of current density, with [20 μm]^2 micropixels showing highest peak EQE and better thermal/electrical performance.

Figure 4. (a) FDTD-simulated normalized light extraction efficiency (LEE) comparison between nanopixel arrays (vertical and tapered) and planar micropixel structures, showing ~3– 4× fold improvement for nanopixels. (b) Simulated far field emission patterns of the vertical and tapered nanopixel structures which show emission directionality.

Figure 5. (a) Tilted-view SEM image of top-down fabricated AlGaN UV-C nanopixels after KOH wet etching, showing inverted trapezoid profiles. (b) High-magnification SEM of etched-back nanopixel array planarized in spin-on glass (SOG), highlighting residual surface openings between the top *p*-GaN and SOG layer in the inset. (c) Cross-sectional SEM image of the full device structure with the Ni/Au *p*-Contact. (d) HAADF-STEM image of the sidewalls of the UV-C nanopixels after wet etching step, showing good crystallinity. (e) High magnification HAADF image of the region corresponding to the red dashed box in (d), showing the UV-C emitting MQW region. (f) Schematic illustration of the UV-C nanopixel device.

Figure 6. (a) *J–V* characteristics comparing nanopixel array with planar [20 μm]^2 micropixel device. Inset: log-scale view of subthreshold behavior in nanopixels due to current leakage via SOG residual openings. (b) EL spectra of the nanopixel array under injection currents from 15 to 1000 A/cm^2, showing stable and bright UV-C emission. (c) Normalized EL spectra of nanopixel vs. planar micropixel at 1000 A/cm^2, with narrower FWHM in nanopixels indicating enhanced optical confinement and emission directionality.

Figure 7. (a) Measured light output power (LOP) density for [20 μm]^2 nanopixel and micropixel devices. Nanopixel array exhibits >10 W/cm^2 LOP density. The measured LOP density is ~4× lower than planar micropixels. Inset: light output power measurement setup, where the device is mounted on top of a calibrated photodiode and the emitted UV-C light is collected through the backside of the sapphire substrate (b) External quantum efficiency (EQE) comparison showing a peak EQE of 1.01% for [20 μm]^2 nanopixel device. The reduction in EQE relative to micropixels is primarily due to absorption in the spin-on glass (SOG) planarization layer. Inset: optical microscope image of the nanopixel device at ~100 A/cm^2 (c) UV–visible absorption spectra comparing a bare AlGaN UV-C LED die and an UV-C LED die coated with cured spin-on-glass (SOG). The SOG-coated sample exhibits ~3× higher absorption at 275 nm, indicating parasitic absorption/losses in the UV-C range. (d) Overlay of normalized absorption spectra with normalized electroluminescence (EL) spectra from the UV-C LED devices.

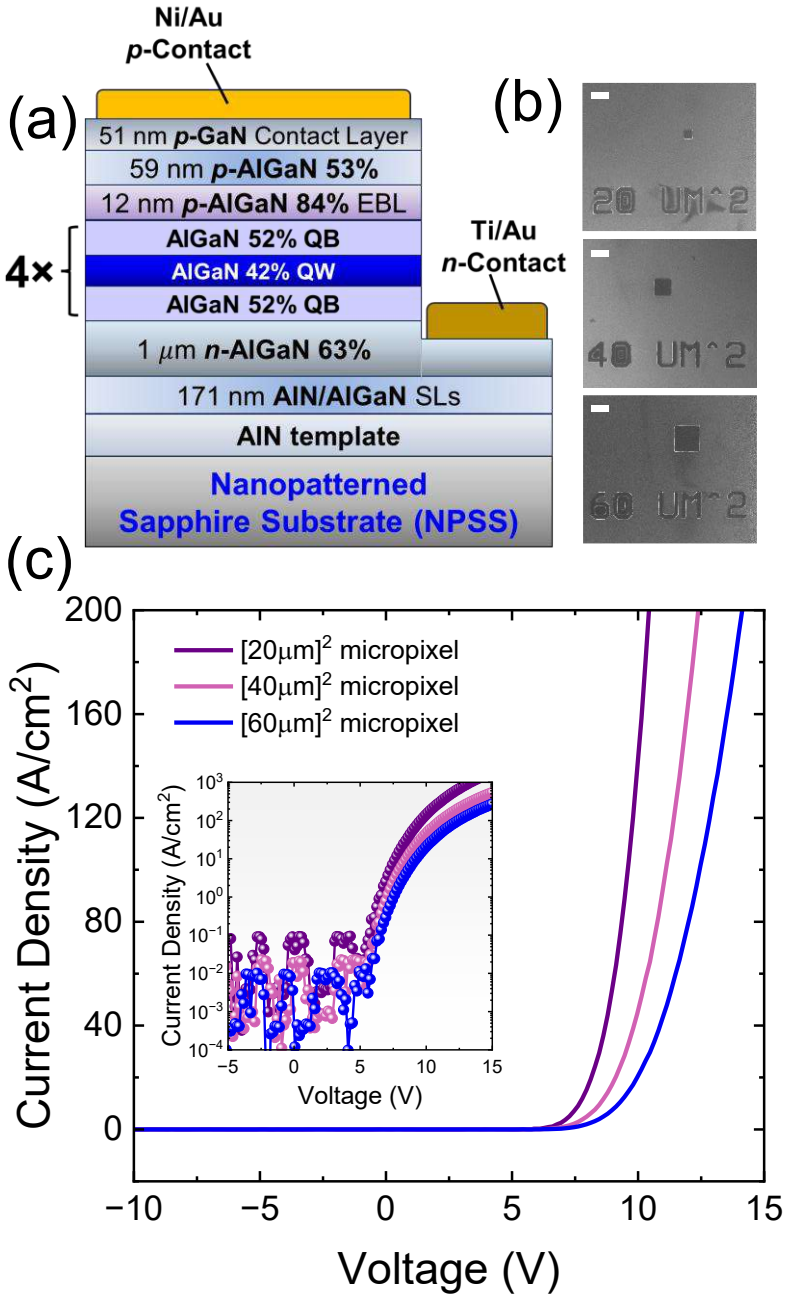

(a)
Ni/Au
p-Contact
51 nm p-GaN Contact Layer
59 nm p-AlGaN 53%
12 nm p-AlGaN 84% EBL
4×
AlGaN 52% QB
AlGaN 42% QW
AlGaN 52% QB
Ti/Au
n-Contact
1 μm n-AlGaN 63%
171 nm AlN/AlGaN SLs
AlN template
Nanopatterned
Sapphire Substrate (NPSS)
(b)
20 UM^2
40 UM^2
60 UM^2
(c)
[20μm]2 micropixel
[40μm]2 micropixel
[60μm]2 micropixel
Current Density (A/cm2)
Voltage (V)

Figure 1

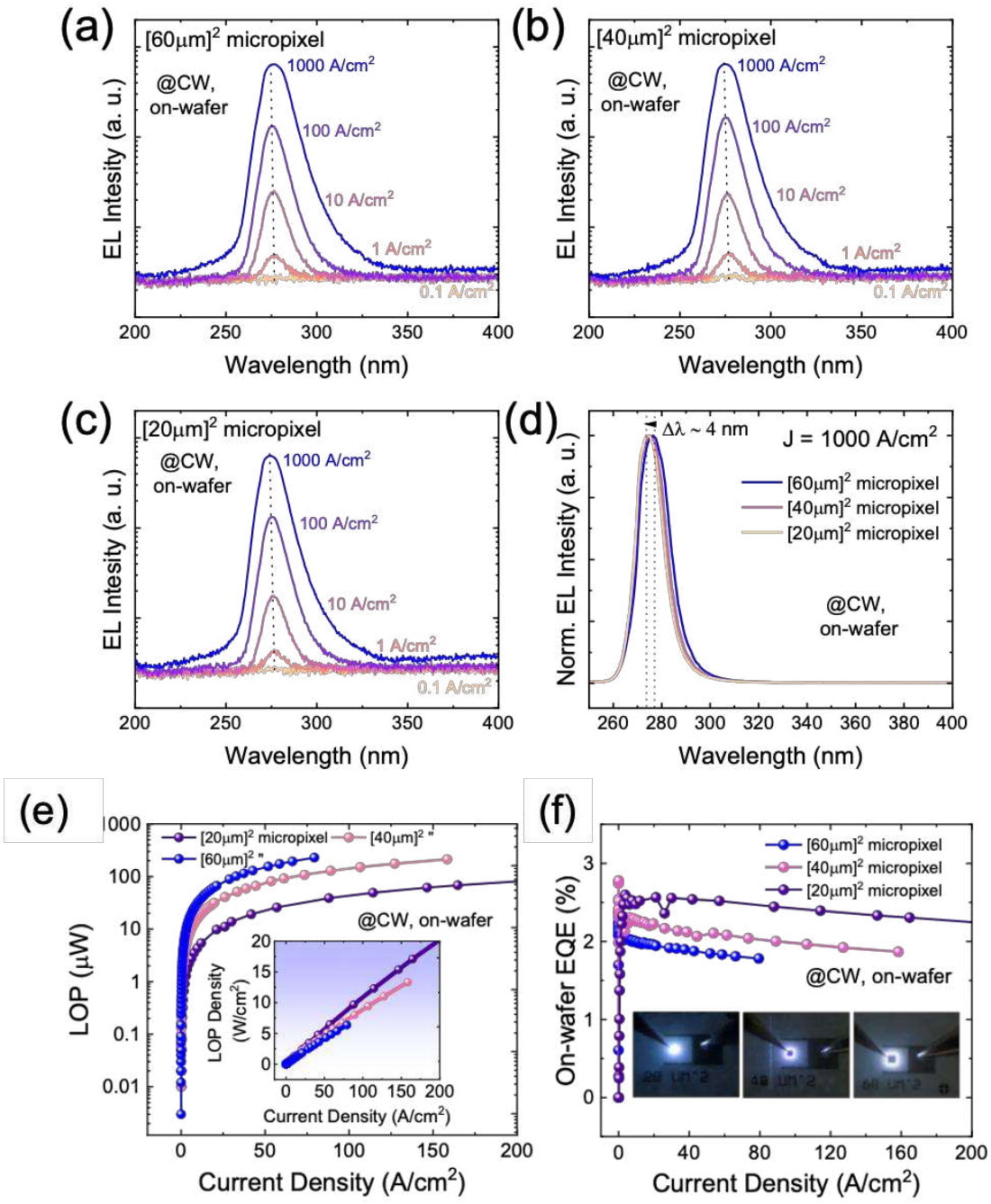

(a)
[60μm]² micropixel
@CW, on-wafer
1000 A/cm²
100 A/cm²
10 A/cm²
1 A/cm²
0.1 A/cm²
EL Intesity (a. u.)
Wavelength (nm)
(b)
[40μm]² micropixel
@CW, on-wafer
(c)
[20μm]² micropixel
@CW, on-wafer
(d)
Δλ ~ 4 nm
J = 1000 A/cm²
[60μm]² micropixel
[40μm]² micropixel
[20μm]² micropixel
@CW, on-wafer
Norm. EL Intesity (a. u.)
(e)
LOP (μW)
Current Density (A/cm²)
@CW, on-wafer
LOP Density (W/cm²)
(f)
On-wafer EQE (%)
Current Density (A/cm²)
@CW, on-wafer

Figure 2

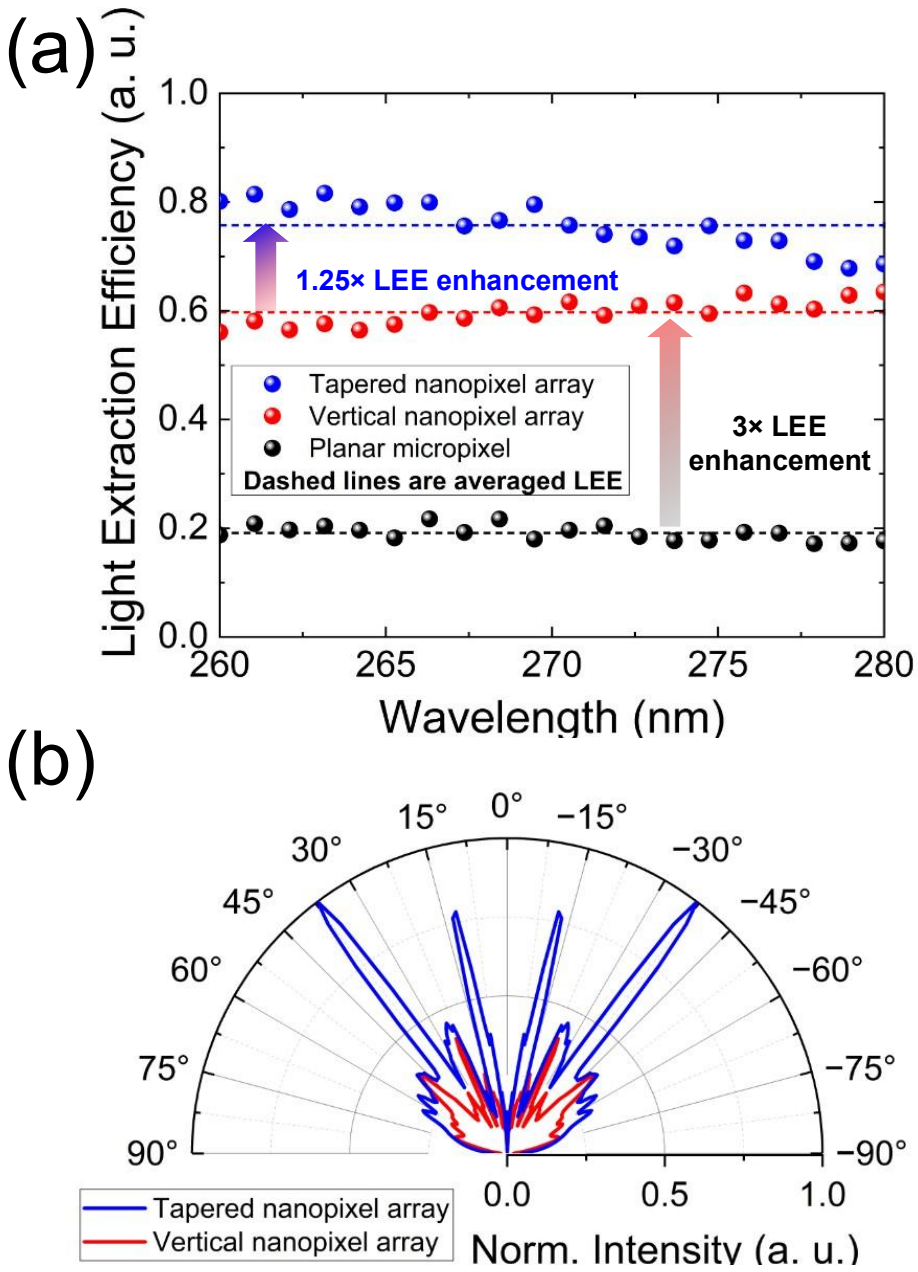

(a)
Light Extraction Efficiency (a. u.)
1.0
0.8
0.6
0.4
0.2
0.0
260
265
270
275
280
Wavelength (nm)
1.25× LEE enhancement
3× LEE enhancement
Tapered nanopixel array
Vertical nanopixel array
Planar micropixel
Dashed lines are averaged LEE
(b)
0°
15°
−15°
30°
−30°
45°
−45°
60°
−60°
75°
−75°
90°
−90°
0.0
0.5
1.0
Norm. Intensity (a. u.)
Tapered nanopixel array
Vertical nanopixel array

Figure 3

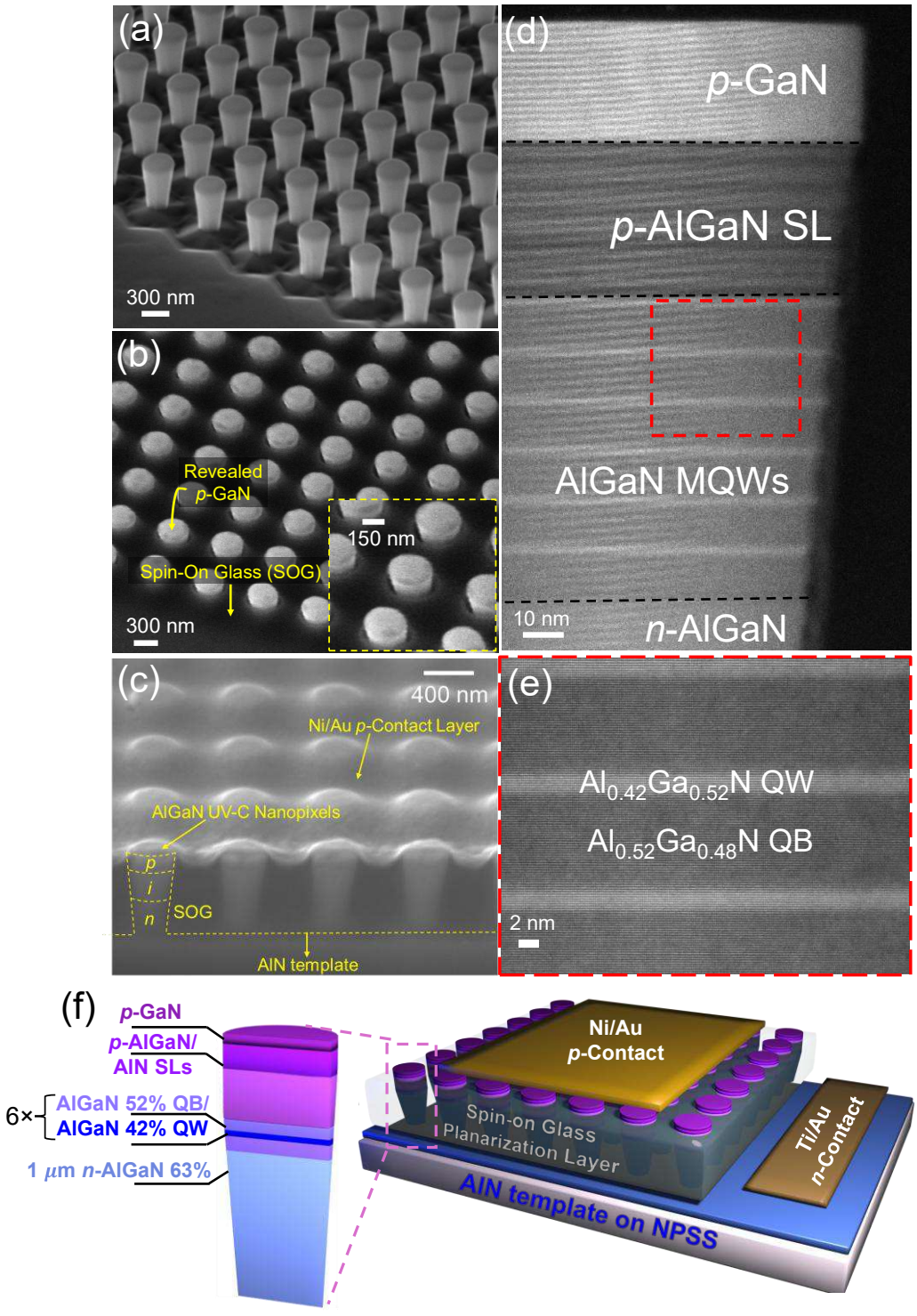

(a)
300 nm
(b)
Revealed
p-GaN
Spin-On Glass (SOG)
150 nm
300 nm
(c)
400 nm
Ni/Au p-Contact Layer
AlGaN UV-C Nanopixels
p
i
n
SOG
AlN template
(d)
p-GaN
p-AlGaN SL
AlGaN MQWs
10 nm
n-AlGaN
(e)
Al0.42Ga0.52N QW
Al0.52Ga0.48N QB
2 nm
(f)
p-GaN
p-AlGaN/
AlN SLs
6×
AlGaN 52% QB/
AlGaN 42% QW
1 μm n-AlGaN 63%
Ni/Au
p-Contact
Spin-on Glass
Planarization Layer
Ti/Au
n-Contact
AlN template on NPSS

Figure 4

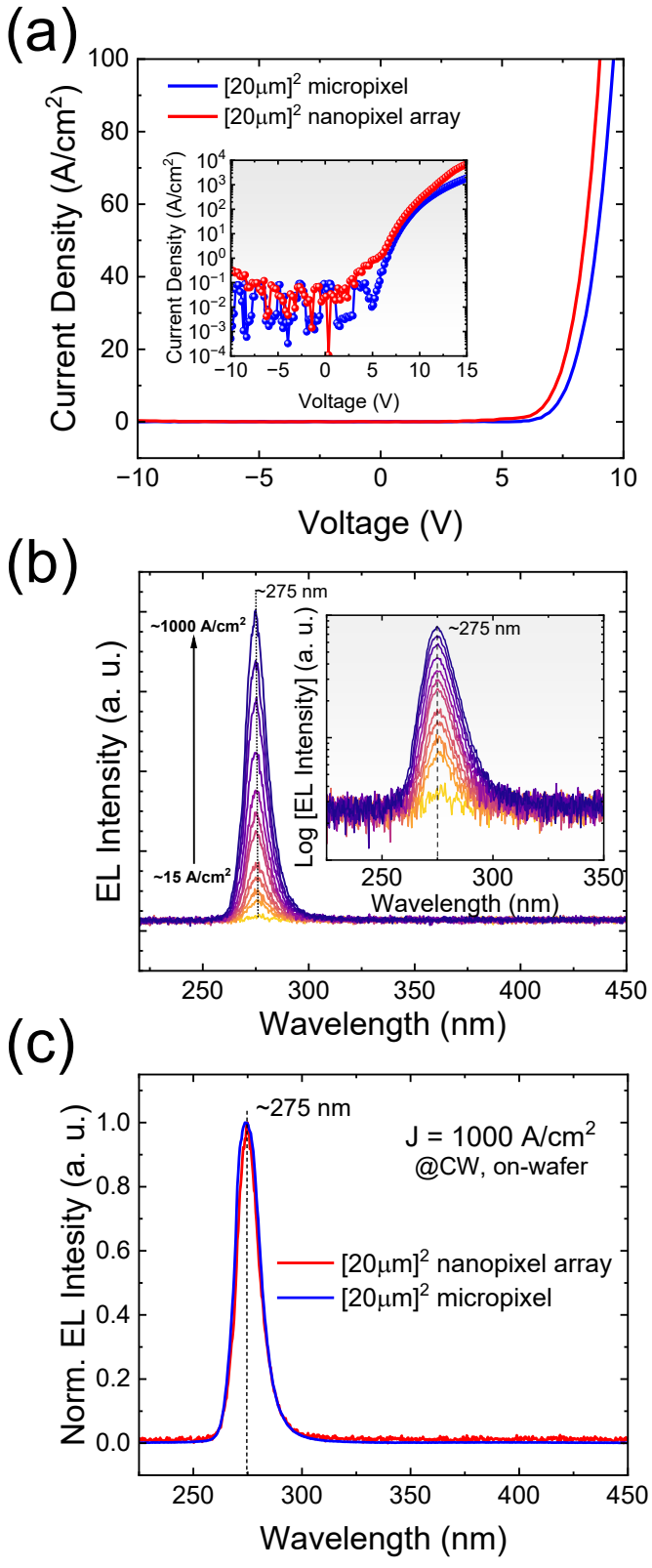

(a)
Current Density (A/cm^2)
Voltage (V)
[20μm]^2 micropixel
[20μm]^2 nanopixel array
Current Density (A/cm^2)
Voltage (V)
(b)
EL Intensity (a. u.)
Wavelength (nm)
~275 nm
~1000 A/cm^2
~15 A/cm^2
Log [EL Intensity] (a. u.)
~275 nm
Wavelength (nm)
(c)
Norm. EL Intesity (a. u.)
Wavelength (nm)
~275 nm
J = 1000 A/cm^2
@CW, on-wafer
[20μm]^2 nanopixel array
[20μm]^2 micropixel

Figure 5

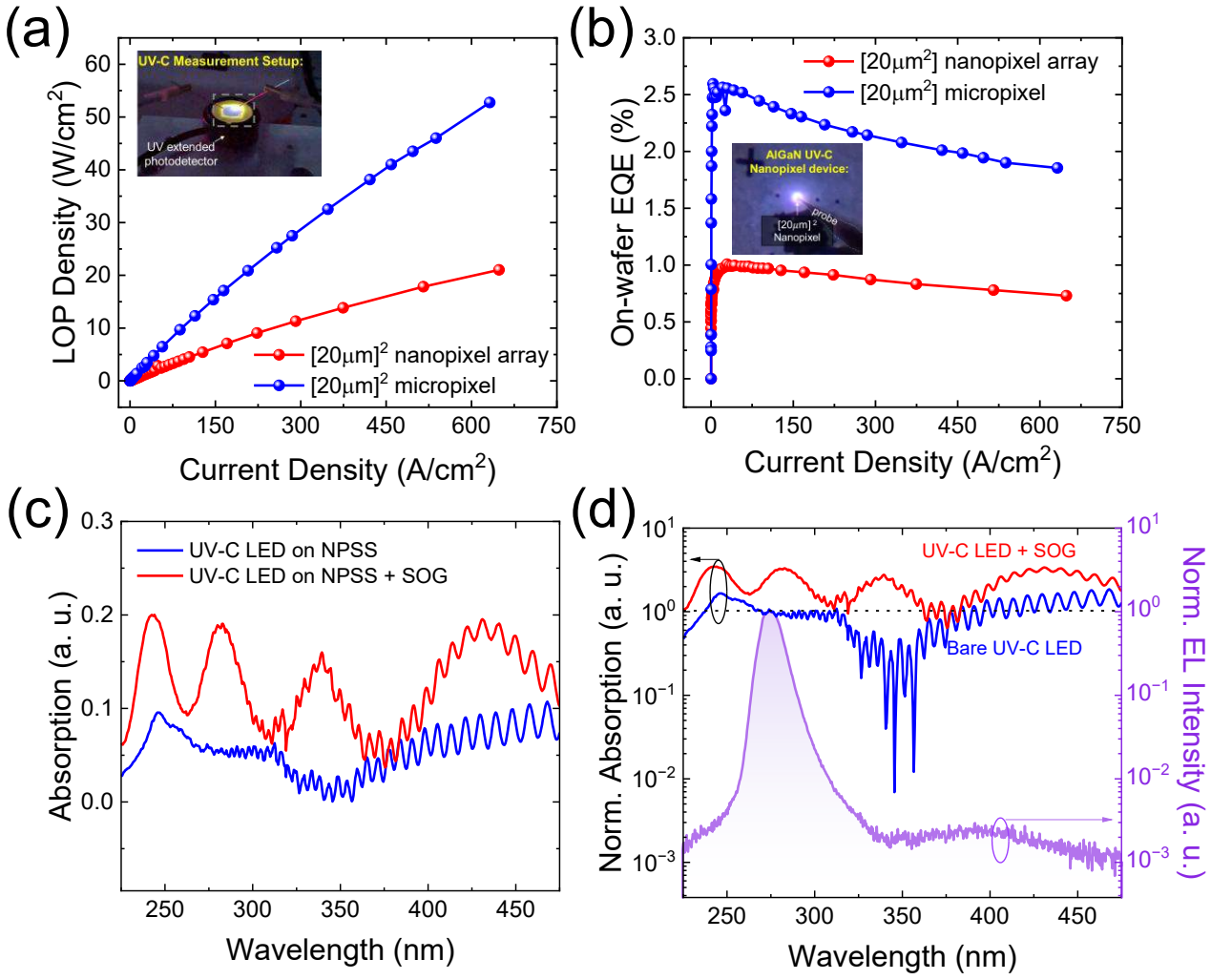

(a)
UV-C Measurement Setup:
UV extended photodetector
LOP Density (W/cm^2)
Current Density (A/cm^2)
[20μm]^2 nanopixel array
[20μm]^2 micropixel
(b)
[20μm^2] nanopixel array
[20μm^2] micropixel
AlGaN UV-C Nanopixel device:
probe
[20μm]^2 Nanopixel
On-wafer EQE (%)
Current Density (A/cm^2)
(c)
UV-C LED on NPSS
UV-C LED on NPSS + SOG
Absorption (a. u.)
Wavelength (nm)
(d)
UV-C LED + SOG
Bare UV-C LED
Norm. Absorption (a. u.)
Norm. EL Intensity (a. u.)
Wavelength (nm)

Figure 6

Supplementary Files

This is a list of supplementary files associated with this preprint. Click to download.

- ReformattedSupportingInformationUVCNanopixels2026.docx
- TABLEOFCONTENTGRAPHIC.png